Intradecadal variations in length of day: Coherence with models of the Earth's core dynamics

Séverine Rosat, Nicolas Gillet

Highlights

Intradecadal variations in length of day: coherence with models of the Earth's core dynamics

S. Rosat, N. Gillet

- After zonal tides removal, the atmosphere and the core are the main contributors to intradecadal changes in length-of-day.
- Smaller contributions of continental and ocean water mass redistributions are mostly compensated by sea level variations.
- Three periodic oscillations have been highlighted in LOD observations at about 6, 7 and 8.5 years.
- The atmospheric contribution is subdominant at periods longer than 5 yr.
- Coherence with core flow models suggest a core origin for the 6 and 8.5-yr oscillations.
- Our synthetic tests suggest that the previously documented 7-yr line could result from an artefact.
- Two coherent oscillations around 3.5 and 5-yrs are conspicuous in the observed LOD and core-flow predicted LOD.
- Torsional Alfvén waves or QG-MC waves are natural explanations to the presence of various interannual signals in the LOD.

Intradecadal variations in length of day: coherence with models of the Earth's core dynamics

S. Rosat[a,*], N. Gillet[b]

[a] *Universite de Strasbourg, CNRS, Institut Terre et Environnement de Strasbourg, UMR 7063, 5 rue Descartes Strasbourg, France*
[b] *Universite de Grenoble Alpes, Univ. Savoie Mont Blanc, CNRS, IRD, UGE, ISTerre, Grenoble, France*

Abstract

We confirm the presence of interannual oscillations of period about 5.9 and 8.5 years in the Earth's length of day (LOD), better visible after subtracting the atmospheric contribution. Continental water mass redistribution and oceanic angular momentum contribute to a lesser extent, and are furthermore mostly compensated by sea level variations. We show, using a continuous wavelet transform analysis of synthetic oscillators embedded into a random correlated noise, the limits of isolating damped signals presenting nearby periods in time series of limited duration. In particular, we emphasize the possibility that a previously documented 7.3-year oscillation could be an artefact associated with the restricted available time span covered by LOD data. Finally, we perform a wavelet coherence analysis between geodetically observed LOD changes and their prediction from geomagnetically inferred core flow models. It confirms an origin from the fluid outer core for the two signals around 5.9 and 8.5 years. A convincing coherence is also found around 3.5 and 5 years, which may reveal signatures of higher harmonics of torsional modes or of quasi-geostrophic magneto-Coriolis modes.

Keywords: length of day, core flows, damped oscillators, wavelet coherence

1. Introduction

In the recent years, several studies have highlighted the presence of interannual periodic signals in the variations of length of day (LOD). An oscillation of period close to 6 years, hereafter referred as SYO, first detected by Abarca del Rio et al. (2000), has been admitted to originate from the core, in particular given its correlation with the occurrence of geomagnetic jerks, or abrupt changes in the rate of change of the magnetic field (Holme and De Viron, 2013), and its convincing prediction by core flows inverted from independent magnetic observations (Gillet et al., 2010). The analysis of such motions have led Gillet et al. to propose torsional Alfvén waves propagating in the fluid outer core as a possible physical mechanism behind the SYO in the LOD signal. These constitute a natural oscillatory response within the rapidly rotating spherical core permeated by the

*severine.rosat@unistra.fr

Published in Physics of the Earth and Planetary Interiors https://doi.org/10.1016/j.pepi.2023.107053

geomagnetic field (Braginskiy, 1970). Organized in cylinders whose axis is aligned with the Earth's rotation vector, such axisymmetric motions can carry angular momentum in the presence of a non-zero core-mantle coupling (Jault and Finlay, 2015), and thus possibly generate a signal in the LOD series. Several mechanisms have been proposed for the coupling, amongst which a gravitational torque involving a non-spherical inner core and mass anomalies in the mantle (Mound and Buffett, 2006; Chao, 2017), or an electromagnetic coupling due to a finite conductance of the lowermost mantle (e.g., Jault, 2003; Schaeffer and Jault, 2016).

The SYO is best seen after removing the contribution from the atmospheric angular momentum (Abarca del Rio et al., 2000; Duan et al., 2015). Its stability over time has been debated (Holme and De Viron, 2013; Chao et al., 2014; Gillet et al., 2015), in link with the finite duration of accurate LOD series (preventing from precisely characterizing modulations, or dissociating several possible spectral lines around the 6-yr period). In more recent years, thank to the increasing length of the LOD series, several studies have highlighted the presence of distinct oscillations besides the SYO, at periods around 8.6-year (Duan and Huang, 2020) and 7.3-year (Hsu et al., 2021). The 8.6-year signal is hereafter referred to as the EYO (Eight-Year Oscillation).

The SYO and EYO are convincingly predicted by recent core flow models inferred from magnetic data (Istas et al., 2023). Torsional modes may be natural candidates, in particular as their periods are not necessarily integer fraction of the fundamental mode (Gillet et al., 2017). With the recent discovery of quasi-geostrophic Magneto-Coriolis modes at interannual periods (Gillet et al., 2022), an alternative possibility arises. These motions are proposed to be at the source of interannual magnetic field changes highlighted from satellite records over the past two decades (Chulliat and Maus, 2014; Finlay et al., 2016). Predominantly non-axisymmetric, they may nevertheless contain a zonal contribution and thus carry angular momentum (Istas et al., 2023). This would provide an explanation for the concomitance found between jerks and LOD variations (Holme and De Viron, 2013; Duan and Huang, 2020), also observed in geodynamo simulations approaching Earth-like conditions (Aubert and Finlay, 2019; Aubert et al., 2022).

For the last signal at 7.3-year period, no mechanism has been discussed so far. The above three signals have been described as damped oscillators, with associated decaying or increasing times longer than the period by about one order of magnitude (about 100 and 60 years for respectively the SYO and EYO, see Duan and Huang, 2020). Meanwhile, the finite length of the available series raises the question of the frequency resolution. The time span covered by accurate VLBI data (started in 1962) is today $\Delta T \simeq 60$ years. Following the Rayleigh criterion for undamped harmonic oscillations (Godin, 1972), around a given period T_0 the resolution in period is $\delta T \approx 2T_0^2/\Delta T$. For $T_0 = 5.9$ years, it gives $\delta T \approx 1.2$ year: if we can today convincingly distinguish the SYO from the EYO, the 7.3-year signal marginally separates from the latter two, and the question of its resolution can be raised.

In the present study we show, using stochastic damped harmonic oscillators embedded into a random correlated noise, the limits of detecting and isolating quasi-periodic signals with nearby frequencies in series of limited duration. We employ a continuous wavelet transform (CWT) method, which is best suited for the analysis of transient signals. The CWT is then applied to geodetically observed LOD data, and to geomagnetically predicted LOD variations from core flow models. A wavelet coherence analysis is finally applied to estimate the coherency and phase lag between the predicted and observed

oscillations. We show conclusive coherences for the SYO and EYO. Higher frequency coherent signals, of weaker amplitude, are also conspicuous around 3.5 and 5 years. We finally conclude that the core flow variations can explain the SYO and EYO found in LOD observations.

2. Description of geophysical data and methods

2.1. Geodetic LOD data and surface geophysical fluid products

LOD data considered here result from the concatenation of the Lunar97 series (Gross, 2001) prior to 1962, together with the C04 series (Bizouard and Gambis, 2009) from 1962 onwards. This latter is provided by the International Earth Rotation and Reference System Service (IERS). It has been first cleaned for solid zonal tides (following IERS Conventions, 2010). For their combination, Lunar97 and C04 have been shifted in such a way that they share the same average over the common era 1962–1997. The LOD series have been furthermore corrected for contributions from atmospheric angular momentum using NCEP/NCAR model (Barnes et al., 1983) from the IERS. An observed 1.4 ms/cy centennial trend (Stephenson et al., 1984) was fitted and removed for the time-span considered. Surface fluid layers angular momentum functions are provided since 1976 by the Earth System Modelling Data at GFZ (Dobslaw et al., 2010), and from the IERS since 1962. For time span between 1948 and 1976, only atmospheric correction can be performed using NCEP/NCAR model (Barnes et al., 1983). The ECMWF and NCEP/NCAR models turn out to be in good agreement at interannual periods on their common time-span with a standard deviation of their difference of 0.01 ms. The LOD and the several contributions from external envelopes are illustrated in Fig. 1(a), starting from 1976.

The effective angular momentum functions due to mass transport processes in atmosphere (AAM – atmospheric angular momentum), oceans (OAM – oceanic angular momentum), and the continental hydrosphere (HAM – hydrological angular momentum) are provided with a temporal resolution of down to 3 hours and include the matter and motion terms. OAM is extracted from the ECCO reanalysis (Estimating the Circulation and Climate of the Ocean) by JPL between 1962 and 1976 (Wunsch et al., 2009), and from the Max-Planck-Institute for Meteorology Ocean Model (MPIOM, Jungclaus et al., 2013). HAM is provided from the Land Surface Discharge Model (LSDM, Dill, 2008).

The consideration of the global mass balance effects is important for seasonal variations in LOD (Yan and Chao, 2012). The barystatic sea level angular momentum (SlAM) is computed by globally integrating masses in ECMWF and LSDM so that the total mass in atmosphere, oceans, and all land storages should be constant at any given time. Eventually missing mass is further assumed to be stored in the oceans only so any net-inflow of water masses into the oceans will cause a barystatic increase in ocean mass (Dobslaw and Dill, 2018). We observe that barystatic sea level changes nearly compensate with HAM and OAM at interannual time scales (see Fig. 1(b)). Besides, they are available only after 1976. Consequently, we removed only NCEP AAM from LOD changes (Fig. 1(c)) in the following analyses, keeping in mind that HAM may contain some remaining unbalanced contributions at interannual periods.

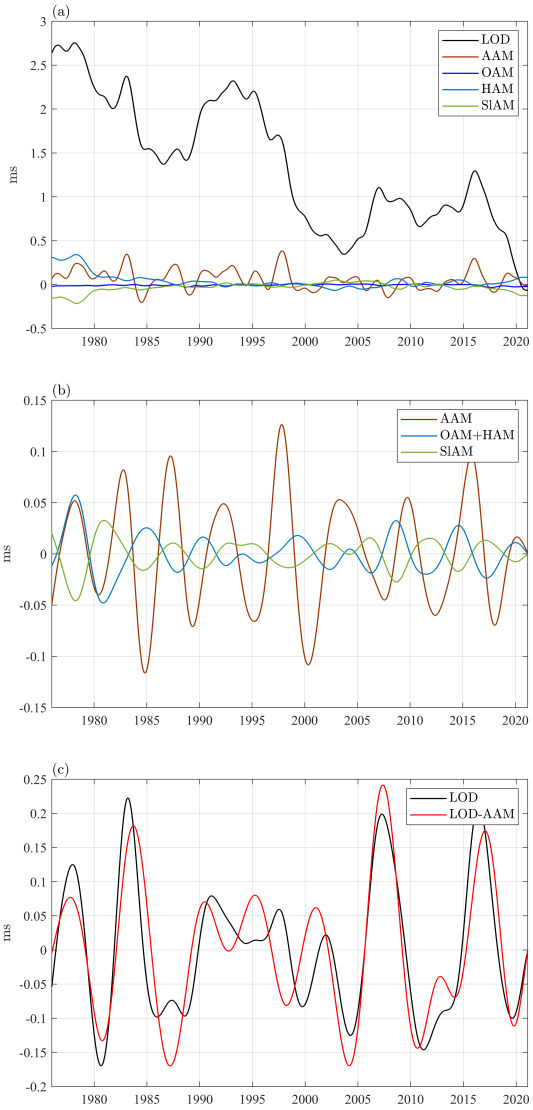

Figure 1: Time series of C04 LOD data, ECMWF atmospheric (AAM), ECCO+MPIOM oceanic (OAM), LSDM hydrologic (HAM) and LSDM-ECMWF sea-level (SlAM) angular momentum functions (1976-2020). (a) Low-pass filtered at 2 year period; (b) AAM, OAM+HAM and SlAM band-pass filtered between 4 and 10 year periods; (c) LOD and LOD-AAM, band-pass filtered between 4 and 10 year periods.

2.2. Synthetic time-series from auto-regressive processes

2.2.1. Synthetic damped oscillators and background series

For the generation of synthetic series, we consider a set of damped oscillators $y_i(t)$ embedded into a background $y_b(t)$ that mimics the long period changes, plus a correlated noise $y_n(t)$. All are obtained by the integration of stochastic differential equations, as described below. We use linear auto-regressive (AR) processes of order 1 (for the noise) or 2 (for the oscillators and the background). The former (resp. latter) have a spectral density which evolve as $S(f) \propto f^{-2}$ (resp. f^{-4}) towards high frequencies. For a general description of such processes, we refer to Yaglom (1962).

A linear AR-2 process $y(t)$ results from an equation of the form

$$\mathrm{d}\frac{\mathrm{d}y}{\mathrm{d}t} + 2\chi \mathrm{d}y + \omega^2 y \mathrm{d}t = \mathrm{d}\zeta\,, \tag{1}$$

with ζ a Wiener process, and (ω, χ) two frequencies. For $\chi^2 < \omega^2$, $y(t)$ takes the form of a damped oscillator, with a covariance function of the form

$$\rho(\tau) = \sigma^2 \exp\left(-\chi|\tau|\right) \left[\cos(\beta\tau) + \frac{\chi}{\beta}\sin(\beta|\tau|)\right]\,, \tag{2}$$

where τ is the time lag, σ^2 the variance of the process and $\beta = \sqrt{\omega^2 - \chi^2}$ the pulsation of the oscillator. When this latter is much higher than the decay rate χ, or $\omega \gg \chi$, one has $\beta \approx \omega$ and

$$\rho(\tau) \approx \sigma^2 \exp\left(-\chi|\tau|\right)\cos(\omega\tau)\,. \tag{3}$$

The quality factor of the process,

$$Q = \omega/(2\chi) = \frac{\pi\tau}{T}\,, \tag{4}$$

is a measure of the number of periods $T = 2\pi/\omega$ per decay time $\tau = 1/\chi$. The several oscillators $y_i(t)$ are each characterized by three parameters: their variance σ_i^2, frequency ω_i and decay rate χ_i. The associated power spectral densities (PSD) are

$$S_i(f) = \frac{4\chi_i\omega_i^2\sigma_i^2}{\left(\omega_i^2 - (2\pi f)^2\right)^2 + \left(4\pi\chi_i f\right)^2}\,, \tag{5}$$

with f the frequency.

The background $y_b(t)$ is also modelled with a process defined by Eq. (1), but in the case where $\omega = \chi$. Then it is only defined by two parameters: its variance σ_b^2 and a cut-off frequency ω_b. Its correlation function is

$$\rho_b(\tau) = \sigma_b^2\left(1 + \omega_b|\tau|\right)\exp\left(-\omega_b|\tau|\right)\,, \tag{6}$$

and its PSD is

$$S_b(f) = \frac{4\omega_b^3\sigma_b^2}{\left(\omega_b^2 + (2\pi f)^2\right)^2}\,. \tag{7}$$

This choice is made to mimic the behavior of the long period LOD signal (see Fig. 1(a)).

Finally the correlated noise is modeled through an AR-1 process, of the form

$$\mathrm{d}y + \omega_n y \mathrm{d}t = \mathrm{d}\zeta \,. \tag{8}$$

It only depends on two parameters, a variance σ_n^2 and a restoring frequency ω_n, which define its correlation function

$$\rho_n(\tau) = \sigma_n^2 \exp\left(-\omega_n|\tau|\right) \,. \tag{9}$$

Sampled at a frequency $f \gg \omega_n$, the process behaves like a random walk, whereas for $f \ll \omega_n$ it is like a white noise. Such processes are characterized by a PSD of the form

$$S_n(f) = \frac{2\omega_n\sigma_n^2}{\omega_n^2 + (2\pi f)^2} \,. \tag{10}$$

This choice is made to mimic the high frequency behavior of the LOD once cleaned for the contributions from the atmosphere and the solid tides.

We shall consider below synthetic series made of the sum of 3 damped oscillators, a background and a noise. This configuration (together with the parameters for each of the processes), is chosen in order to approximately replicate the spectral content of the observed LOD as measured with geodetic data once cleaned for the atmospheric contribution (see Fig 2). The favored parameters are the following: $(T_1, T_2, T_3) = (6, 8.5, 17)$ yr, $(Q_1, Q_2, Q_3) = (20\pi, 20\pi, \pi)$, and $(\sigma_1, \sigma_2, \sigma_3) = (0.1, 0.08, 0.4)$ ms for the three damped oscillators, $\omega_b = 1/15$ yr^{-1} and $\sigma_b = 1$ ms for the background, $\tau_n = 1$ yr and $\sigma_n = 0.04$ ms for the noise. We acknowledge that there is some flexibility in the above parameters (in particular concerning τ_n or ω_b). We consider a single oscillator at decadal periods for the sake of simplicity, even though there may exist more than one (e.g., Chao et al., 2014). However, we attempt here at generating a set-up as simple as possible, still being representative of the PSD witnessed with observed series. The superposition of the PSD for synthetic and geodetic data from 60 yr long series does not call for a larger complexity.

The theoretical PSD for the several synthetic contributions is shown in Fig. 3 (top) for the above choice of parameters. It clearly illustrates the domination of the noise towards short periods, of the background towards long periods, while the sharpness of the three oscillators is much more clear that on the PSD obtained with 60 yr long series. One example of synthetic series, with the parameters chosen above, is provided in Fig. 3. In practice, we generate the discrete synthetic series over a time interval ΔT and with a sampling period δt. These are stored in vectors $\mathbf{y}_i, \mathbf{y}_b, \mathbf{y}_n$ for the oscillators, the background and the noise, of size $N = \Delta T/\delta t + 1$. To this purpose we calculate from the function (2) the covariance matrix $\mathsf{C}_i = \mathbb{E}\left(\mathbf{y}_i\mathbf{y}_i^T\right)$, where $\mathbb{E}\left(\dots\right)$ means the statistical expectation. The processes are assumed to have a priori a zero mean. Random discrete series are then obtained by multiplying the Choleski decomposition L_i of $\mathsf{C}_i = \mathsf{L}_i\mathsf{L}_i^T$ with $\mathbf{w}$ a random Gaussian vector of size N, unit variance and zero mean. The same process is used to obtain $\mathbf{y}_b$ and $\mathbf{y}_n$ from Eq. (6) and (9), respectively.

2.2.2. Prior insights from continuous wavelet transform

Duan et al. (2015) have extracted the SYO from the LOD series between 1962 and 2012, using a normal Morlet wavelet method (Morlet et al., 1982; Liu et al., 2007). Then, using the same wavelet method, Duan et al. (2017) estimated the damping rate of the

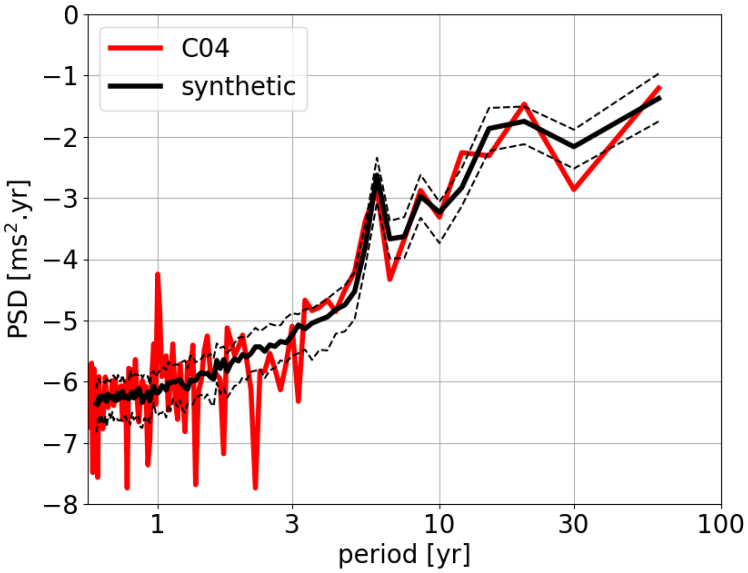

Figure 2: In red the PSD of the C04 series (1962–2022) cleaned for NCEP AAM and solid tides (IERS Conventions, 2010). It is superimposed with the median PSD (in black) within an ensemble of 100 synthetic stochastic series with the same 60 yr duration. The dotted black lines indicate the 25% and 75% quantiles within the ensemble of synthetic series. Parameters of the stochastic processes have been chosen so as to match the LOD data PSD with that of the median synthetic series (see text for details). The PSD is computed after applying a Kaiser window on each of the series, with shape parameter $\beta = 2.5$.

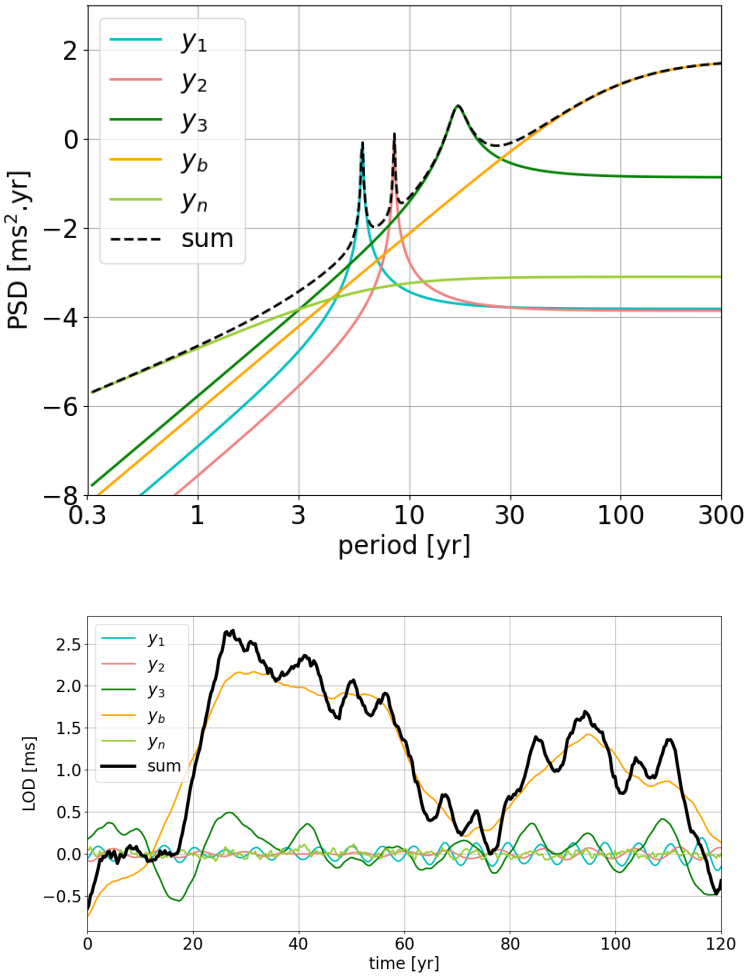

Figure 3: Analytical PSD (top) and one example of synthetic stochastic series (bottom) corresponding to the set up favored from Fig. 2. The several contributions from the 3 damped oscillator ($y_{1...3}$, of periods 6, 8.5 and 17 yr), the noise and background have been isolated (see text for details).

SYO with a quality factor of $Q \sim 50$ (a decay time of about 100 yr) by least-squares fitting a decaying sinusoidal function in the time domain. Duan and Huang (2020) highlighted, on top of a SYO, the presence of a EYO presenting a good concordance with the occurrence of geomagnetic jerks. They however obtained an increasing signal by fitting an exponential function in time-domain with a rate of about 1/60 yr (or $Q \approx 20$). They provided values for the average amplitudes of the SYO and EYO, at respectively $\sim$0.12 and $\sim$0.08 ms over 1962–2018. Hsu et al. (2021) have proposed a frequency domain stepwise regression method to identify and characterize periodic signals. They have tested their method on synthetic data composed of three oscillators at 5.9, 7.3 and 8.5-year periods with respective amplitudes 0.12, 0.05 and 0.08 ms. They have also tested the case of varying amplitudes with a quality-factor of $Q \sim 50$ for the SYO and an increasing amplitude for the EYO, while the 7.3-year oscillation was kept steady. For some tests, these oscillations were buried in a white noise of standard deviation 0.025 ms. They have employed their method on actual LOD data, and proposed the existence of three components at 5.9, 7.3 and 8.5-year periods. They further used the normal Morlet wavelet transformation to check the consistency with their protocole.

With short series, estimating Q from a PSD is subject to uncertainties (see Fig. 2). In this context, values of Q proposed so far from the analysis of LOD records have been obtained by fitting analytical functions to the observed series, after filtering. We illustrate below that approaching Q this way might lead to biased estimates. We generated 1000 noise-free series $y(t)$ for a single damped oscillator of frequency f^*, amplitude A^*, and quality factor Q^*, over a duration $\Delta T = 7/f^*$. This time-span is similar to the configuration of a 8.5 yr signal recorded over 60 yr of geodetic LOD data, and has been previously considered short enough for the oscillator to present a behavior characteristic of its theoretical growth or decay (e.g. Duan et al., 2017; Duan and Huang, 2020). We consider below two values $Q^* = 20\pi$ and $Q^* = 40\pi$. We fitted the synthetic series with functions of the form

$$f(t) = A \exp(\alpha t) \cos(2\pi f(t - t_0)) \ . \tag{11}$$

Adjustable parameters are the amplitude A and frequency f of the oscillator, its phase (through t_0) and its decay (or growth) time α. The recovered quality factor is then $Q = \pi f/|\alpha|$. In this relatively simple configuration, the fit allows to retrieve accurately the frequency (with $\pm 1\%$), while the amplitude is over-estimated by $\approx 20\%$ (from the median value, see Table 1). Meanwhile, the inferred Q significantly under-estimates the reference Q^*, and this mis-estimation is stronger for larger values of Q^*; in the case where $Q^* = 40\pi$ the targeted value is only marginally included within the first three quantiles. In many occasions, the sampled oscillator is not in a period characteristic of the expected growth/decay. For the synthetic tests presented in our study, we thus considered instead as geophysically representative empirical series obtained with values of Q producing PSD statistically comparable to the PSD of the observed LOD series (see Fig. 2). In comparison with previous studies, we consider here relatively larger values of Q (which is coherent with Table 1), in particular for the EYO.

2.2.3. Analysis tools

In the following, the influence of the long-period background is reduced using a high-pass filtering with a cut-off period at 10-year. The time-frequency analysis is based on the CWT using an elongated Morlet wavelet. The wavelet equation is written in the

Q^*	A/A^*			f/f^*			Q/Q^*		
20π	0.70	1.19	1.73	0.99	1.00	1.01	0.37	0.70	1.51
40π	0.79	1.21	1.68	0.99	1.00	1.01	0.24	0.48	1.05

Table 1: Evaluation of the exponential fit for the recovery of the parameters of a single damped oscillator of amplitude A^*, frequency f^*, and quality factor Q^*, for two values of Q^*. We considered a set of 1000 series, covering a time-span of $7/f^*$. The three values in each case represent the 1st quantile, the median and the third quantile within the ensemble of series.

frequency domain as

$$h(af > 0) = 2\exp\left(-4\sigma^2\pi^2\frac{(af - s_0)^2}{2}\right), \tag{12}$$

where s_0 is the frequency of the mother wavelet (with $s_0 = 1$ Hz). σ is an elongation parameter that enables to improve the spectral resolution of the Morlet wavelet, resulting in a better separation of close-by periodic oscillations (we chose $\sigma = 4$). In the meantime, the temporal resolution is degraded when the spectral resolution is improved because of Heisenberg's uncertainty principle (or inequality of Gabor). The CWT transform is performed in the Fourier domain following the method described for instance in Torrence and Compo (1998). Contour lines shown below in the scalograms (Fig. 4, 5, 6, etc.) correspond to the 95% confidence levels and the shaded areas represent the cones of influence (masking the regions of the wavelet spectrum for which edge effects become important).

2.3. Core flow models

The link between subdecadal changes in LOD data and core flows inverted from geomagnetic field observations has been demonstrated using various algorithms for the reconstruction of core motions (Gillet et al., 2015, 2019; Istas et al., 2023). Focusing on band-pass filtered flows, Gillet et al. (2015) had not dissociated the SYO from the EYO, presenting modulated interannual LOD series. Only recently Istas et al. (2023) has shown that both signals, considered separately, are convincingly fitted by core flow reconstructions. We consider below two core flow models, obtained using two versions of the `pygeodyn` software (Huder et al., 2019) and two different kinds of geomagnetic data, as detailed below. `pygeodyn` is a data assimilation tool for the reanalysis of the core surface dynamics. It is based on an ensemble Kalman filter (Evensen, 2003), in which the forward integration of the core flow model is operated using stochastic equations. The parameters entering these empirical equations are extracted from the spatio-temporal statistics of a geodynamo simulation (which solved for the primitive momentum, induction and heat equations). For both considered models, the prior statistics have been extracted from the 71%-path dynamo (Aubert and Gillet, 2021). Subgrid induction and diffusion in the model are accounted for via an augmented state approach.

A first model has been obtained from observations that consist of geomagnetic field Gauss coefficients from the CHAOS-7 geomagnetic field model (Finlay et al., 2020) over 1999–2020, warmed-up prior to 1999 using the COV-OBS.x2 model (Huder et al., 2020), starting in 1880. It consists in an ensemble of 50 realisations obtained using `pygeodyn` with the algorithm described in Gillet et al. (2019). It correspond to a model published by Gillet et al. (2022), hereafter referred to as 'GGJx22'.

The second model (hereafter referred to as 'IGFx23') consists in an ensemble of 400 realizations covering the period 1880–2022. It uses an improved version of `pygeodyn` where the "graphical Lasso" has been implemented for the estimation of the forecast covariance matrix that enters the Kalman filter (Istas et al., 2023). For this reanalysis, observations consist of ground records (annual means, since 1997), virtual observatory data since 2000 (see Hammer et al., 2021b,a), and prior to 1997 of Gauss coefficient series from the COV-OBS.x2 model (Huder et al., 2020). Virtual observatory data considered here are annual means from the CHAMP, Oersted and Cryosat-2 missions, and quarter-monthly values from Swarm (after 2014).

Both reanalyzed core flow series have been interpolated using a 0.2 year sampling.

3. Results

3.1. Geophysical data analysis

Among surface envelopes, the atmosphere possesses the largest contribution to LOD changes. Then come the hydrology and oceans signals (see Fig. 1 and Fig. 4). While the AAM shows enhanced energy at periods shorter than 6 years, the hydrology exhibits a broader frequency content in the period range between 2 and 10 years (Fig. 4). We also observe that HAM excitation function has a small but non-negligible contribution to the interannual LOD fluctuations (Fig. 4(c)). Continental hydrology presents an isolated contribution, with an amplitude of 0.01 ms, at a period close to the 7.3-yr documented by Hsu et al. (2021) for LOD data (though of much weaker magnitude).

As expected, subtracting the atmospheric angular momentum contribution considerably reduces the spectral content of geodetic LOD series at periods shorter than 5 years, while it magnifies the EYO and SYO (see Fig. 1(c) and Fig. 5). This suggests that LOD and AAM are predominantly anti-correlated at these periods (as noted already by Rekier et al., 2022), i.e. the atmosphere and the mantle overall rotate in the same direction at these time-scales. As stated in Section 2.1, OAM and HAM are mostly compensated by SlAM. Consequently, the signal seen in HAM around 7.3 yr is not retrieved when considering the LOD series corrected for the AAM only. We recall that the AAM is the only surface correction that is applied in the following.

3.2. Uncertainties of geodetic LOD series and geophysical products

Assessing uncertainties on LOD series and geophysical products is a difficult task, furthermore when searching for errorbars at specific frequencies. Here we consider the dispersion between time-series and products to provide an estimate of the uncertainty level. Several LOD series and two atmospheric models are available from the IERS website. The uncertainty σ related to the AAM reconstruction is computed as the standard deviation obtained by integrating, between 4 and 9.5 years, the Power Spectral Density of the time series residuals. We obtain a value of $\sigma = 0.01$ ms between ECMWF and NCEP/NCAR AAM products. The paired differences between various LOD series are summarized in Table 2. As for the two AAM models, we have computed the variance by integrating, between 4 and 9.5 years, the PSD of the difference on the common time-span. It thus encompasses the periods of both the SYO and the EYO. We also provide for comparison the variance computed in the same way for the individual time-series.

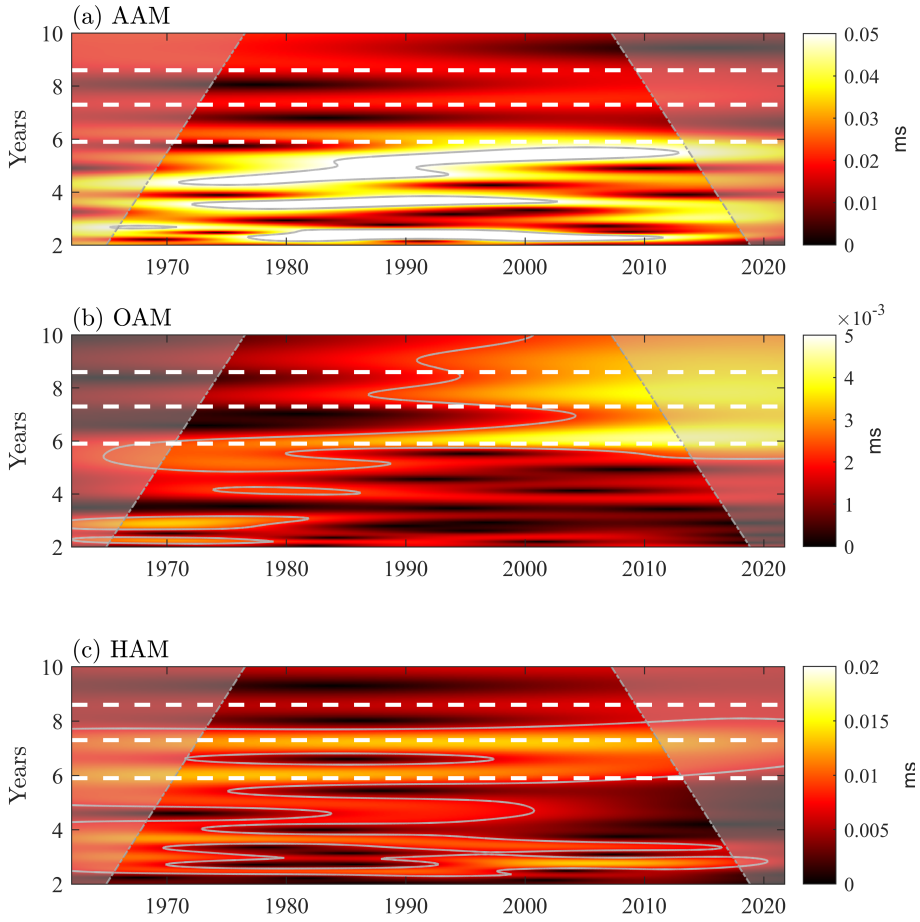

Figure 4: Wavelet transform coefficients of (a) NCEP atmospheric, (b) ECCO+MPIOM oceanic and (c) LSDM hydrologic angular momentum functions (1962-2021). The white dashed lines correspond to the three periods of 5.9, 7.3 and 8.5 yr. Thin white lines represent the 95% confidence level.

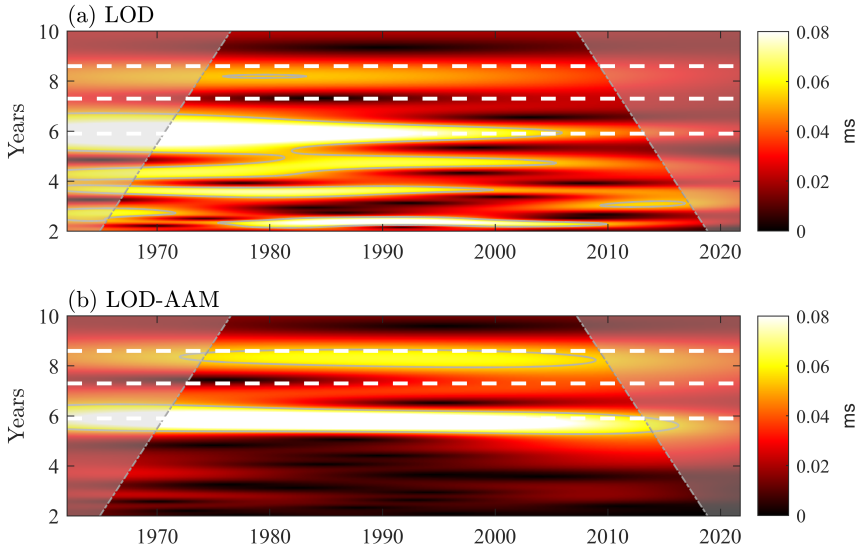

Figure 5: Wavelet transform coefficients of C04 LOD variations (a) only zonal tides were corrected, (b) NCEP atmospheric angular momentum contribution was further subtracted (1962-2021).

We consider the series C01 (IERS), C04 (IERS) and Space (JPL) (defined in the ITRF2020; Altamimi et al. (2023)) that combine various space techniques: VLBI (Very Long Baseline Interferometry), SLR (Satellite Laser Ranging) and GNSS (Global Navigation Satellite Systems). On top of this, the C04 series incorporate Doppler orbitography by radiopositioning integrated on satellite (DORIS) since 2015 (Bizouard et al., 2019), while the Space series consider LLR (Lunar Laser ranging) data (Ratcliff and Gross, 2022). However, the C04 series results mostly from a combined smoothing of LOD GNSS data and UT1 VLBI data. The input of SLR and DORIS LOD values in that combined solution is negligible in reason of their larger uncertainties. We also compare with alternative series, each obtained from a specific technique: the IVS series from VLBI and the JPL series from GNSS. LOD from GNSS provides the smallest differences with other series because of their highest sampling of the Earth's rotation. As expected, combined series C01 and C04 are overall consistent to each other, with a difference coming from a distinct sampling interval (C01 being designed for long-term studies). Larger differences are obtained between IERS C01/C04 and the JPL Space series with $\sigma = 0.12$ ms, only slightly weaker than the r.m.s. of the interannual LOD signal. This estimate is in agreement with previously observed differences (Ratcliff and Gross, 2022), which can be attributed to the following: the C01/C04 series adopt a weighted-average approach to combine geodetic data (Bizouard et al., 2019) while the Space series is based on a Kalman filter, accounting for the growth in the uncertainty of the Earth orientation parameters between measurements (Gross, 2015). Combining various measurement methods is necessary to reduce as much as possible possible technical bias in the estimation of the Earth's rotation parameters. Nevertheless, the difference between C01/C04 and Space is

	C01 (IERS) 1846-2023	C04 (IERS) 1962-2023	Space (JPL) 1993-2023	GNSS (JPL) 1996-2023	VLBI (IVS) 1984-2020
C01 (IERS)	$\mathbf{8 \times 10^{-2}}$	1×10^{-3}	0.12	5×10^{-3}	1×10^{-2}
C04 (IERS)		**0.17**	0.12	6×10^{-3}	1×10^{-2}
Space (JPL)			**0.25**	7×10^{-2}	0.11
GNSS (JPL)				**0.21**	7×10^{-3}
VLBI (IVS)					**0.20**

Table 2: Standard deviations σ (in ms) of the paired differences between astro-geodetic LOD series. σ is computed by integration between 4 and 9.5 years of the PSD of the difference between two time-series on the common time-span. The diagonal values (in bold) are the σ for the corresponding LOD series in the band 4-9.5 years computed by integrating the PSD of those series.

Case No.	Background $(y_3 + y_b)$	high-pass filtered at $T \leq 10$ yr	Oscillators	Figure No.
(1)	Yes	No	y_1	Fig. (6) and (A.3)
(1)	Yes	Yes	y_1	Fig. (A.1) (top)
(1)	No	No	y_1	Fig. (A.2) (top)
(2)	Yes	No	$y_1 + y_2$	Fig. (7)
(2)	Yes	Yes	$y_1 + y_2$	Fig. (A.1) (bottom)
(2)	No	No	$y_1 + y_2$	Fig. (A.2) (bottom)

Table 3: Summary of synthetic signals considered in the different cases, with reference to the corresponding figures. All tests were performed with the same noise properties (y_n), and using same time-span $\Delta T = 60$ yr.

not negligible in comparison with the SYO and EYO oscillations described above, of respective amplitudes 0.1 and 0.08 ms. These later are however larger than the differences between C01/C04 and GNSS or VLBI series between 4 and 9.5 years.

3.3. Synthetic data analysis

We have performed several runs on the synthetic series described in section (2.2.1), using various durations ΔT of the time windows. We highlight below two main configurations with $\Delta T = 60$ years, in the presence of the long-period background y_b, the noise y_n and of the the 3rd oscillator of period 17 yr:

- Case (1) one damped oscillator (y_1) of period 6-yr, amplitude 0.1 ms and quality factor $Q = 20\pi$.
- Case (2) two damped oscillators (y_1 and y_2) of periods 6 and 8.5-yr, with respective amplitudes 0.1 and 0.08 ms, and presenting the same quality factor $Q = 20\pi$.

Further comparisons are presented in Appendix A, either after filtering the long period, or in the absence of a background. The various configurations shown here are summarized in the Table (3).

In the configuration of Case (1), we are able to detect the existing subdecadal oscillator above the confidence level. However, we also detect a parasitic oscillator (false positive) over the whole considered time-span, at a period around 7.5 yr (see Fig. 6).

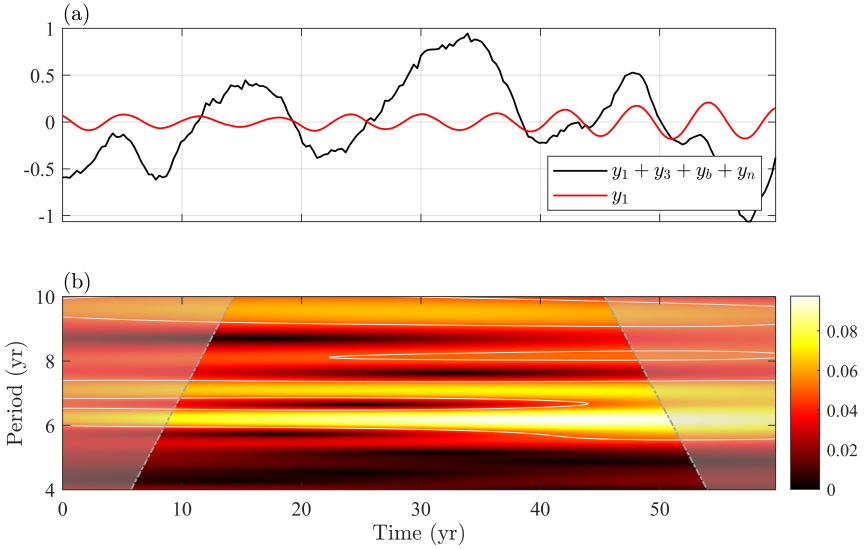

Figure 6: Synthetic signal of Case (1), composed of an auto-regressive stochastic background (y_b) plus two damped oscillators at 6 and 17-yr periods, with $Q = 20\pi$ and $Q = \pi$ (y_1 and y_3) embedded in colored noise (y_n). (a) Time series, (b) Continuous Wavelet Transform.

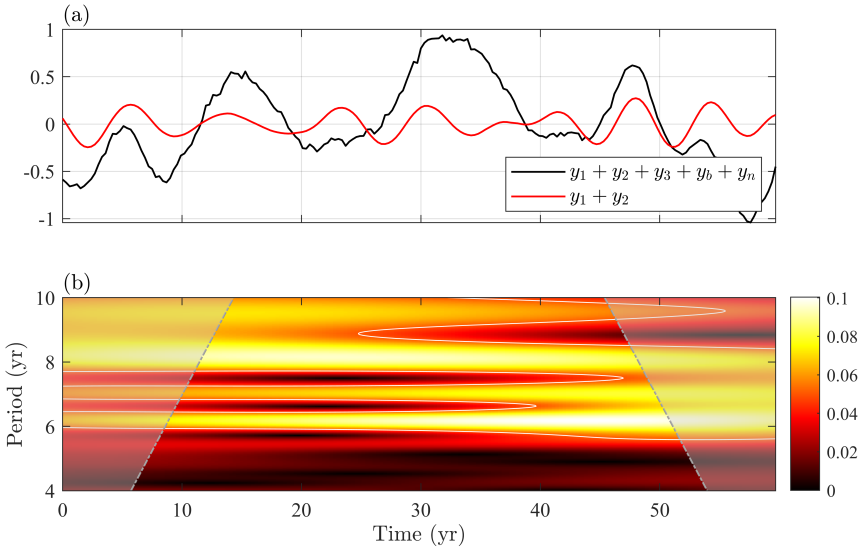

Figure 7: Synthetic signal of Case (2), composed of an auto-regressive stochastic background (y_b) plus three damped oscillators at 6, 8.5 and 17-yr periods embedded in colored noise (y_n). (a) Time series; (b) Continuous Wavelet Transform.

After filtering the low frequency content, the amplitude of the 7.5-year oscillation is reduced but still visible (Fig. A.1). When there is no background, the parasitic 7.5-year oscillation is not visible any more (Fig. A.2). We have considered one hundred runs for generating synthetic oscillators with random starts. Depending on the relative amplitudes of the 6-yr oscillations and the background at the considered epochs, the detection of a parasitic oscillation is more or less obvious (see Fig. A.3). Reducing the duration of the time window and/or decreasing the quality factor Q of the damped oscillator tend to favor the occurrence of false positives.

We now turn to the configuration of Case (2), when two damped oscillators are present at 6 and 8.5 years. We are able to isolate both of them above the confidence level. However, as in Case (1) a parasitic subdecadal oscillation is detected above the confidence level, at an intermediate period ≈ 7 yr (see Fig. 7). When the time-series are high-pass filtered, the parasitic 7-year oscillation is still detected although attenuated (Fig. A.1, bottom), as in Case (1). Here also, when in the absence of a background, we do not see any clear signal emerging around 7-yr periods (Fig. A.2, bottom).

Theoretically, with undamped harmonic signals, we would need $\Delta T > 2T_0^2/\delta T \simeq$ 60 years of data in order to separate a 5.9-yr oscillation from a 7.3-yr oscillation in spectral domain, and $\Delta T \gtrsim 100$ years to separate 8.6-yr and 7.3-yr oscillations, based on the Rayleigh criterion. Our synthetic tests with time duration of 60 years mimic the time duration of LOD records and only marginally respect this criterion for the 5.9 and and 7.3 yr signals. Considering damped oscillators (here with $Q = 20\pi$) renders more difficult the separation of the various spectral lines. In the considered synthetic case, the presence of a background (y_b) and of a decadal oscillator (y_3), both presenting reduced but non-zero power at the subdecadal periods of interest, favors the detection of false positive at a period between 6 and 8.5 yr.

3.4. Coherence analysis with core flows

3.4.1. Oscillations in the period range 4–10 years over 1880–2020

The wavelet coherence is a measure of the correlation between two signals in the time-scale (here time-frequency) domain (t, f) used for the CWT. If we denote $C_x(t, f)$ and $C_y(t, f)$ the wavelet coefficients of the CWT of signals $x(t)$ and $y(t)$, then the wavelet coherence is

$$W_c(t, f) = \frac{C_x^*(t, f)C_y(t, f)}{|C_x(t, f)||C_y(t, f)|} = w_c(t, f) \exp(i\varphi_c(t, f)) \,, \tag{13}$$

with the coherence module $w_c(t, f) \in [0, 1]$ and its phase $\varphi_c \in [-\pi, \pi]$. The superscript * denotes the complex conjugate. As for the CWT, we follow the method described in Grinsted et al. (2004) to implement the wavelet coherence analysis. Coherent signals are characterized by a large module. In the figures below, the phase information is represented via arrows: for two signals in phase, or $\varphi_c = 0$ (resp. opposition phase, $\varphi_c = \pi$), the arrow is oriented to the right (resp. left). For two signals in quadrature ($\varphi_c = \pi/2$) the arrow is oriented upward. In the following, $x(t)$ corresponds to observed LOD variations and $y(t)$ to its prediction from a core flow model. The phase (arrows) are shown only when $w_c \geq 0.3$.

Previous core flow studies (Gillet et al., 2019; Istas et al., 2023) have emphasized the cogent fit between observed and predicted LOD time series. Fig. 8 confronts the

two predictions from models GGJx22 and IGFx23 to geodetic records over 1880–2022. Despite the different ways of accounting for magnetic observations (see Section 2.3), decadal changes are well recovered (except for the early part of the series, when magnetic models are arguably less accurate). It is also the case for interannual variations since 1940: both models overall convincingly predict both the phase and amplitude of the SYO and the EYO observed in LOD data. We pursue the confrontation of LOD data and core flow predictions, and show below the results of the wavelet analysis in the period range $[4, 10]$ years over the time-span 1880–2020 covered by the flow models. In the scalograms of the LOD data (Fig. 9, top), the cleaning of the atmospheric signal after 1948 suppresses a significant part of the observed variability at periods shorter than ~ 5.5 years. The EYO is present starting from ~ 1900, with of amplitude ~ 0.08 ms. Contrary to Hsu et al. (2021) and Duan and Huang (2020), our analysis does not reveal any obvious increase in the amplitude for the EYO. Signals of shorter period are also clearly there from the beginning of the XXth century, with periods ranging from 6 to 7 years and amplitudes similar to that of the EYO. As for the EYO, their signature is less at the beginning of the XXth century. Over the most recent epochs, the period shifts towards that of the SYO.

Despite confidence intervals that are less tightened in period, LOD predictions from both investigated flow models also show enhanced power around 8 and 6 years over the whole time-span, with amplitudes comparable to that of the observed signal – see Fig. 9 (b,c). For both considered models, the period of the predicted EYO is closer to 8 years than 8.5 years. Its amplitude is comparable to the observed one, ~ 0.08 ms (resp. 0.06 ms) for model IGFx23 (resp. GGJx22). The predicted SYO appears more clear starting from ≈ 1940 (as previously noted by Gillet et al., 2019), with for both models an amplitude of about 0.08 ms, similar to the observed one. At periods shorter than ~ 5 years, the predicted LOD shows more power than the observed LOD cleaned from the AAM contribution (i.e., after 1948).

The coherence spectrum analysis presented in Fig. 10 provides additional information regarding the phase of the observed and predicted signals. For both flow models a strong coherence is found for the EYO over the whole time-span (apart from the edges effects), The associated phase presents a negative off-set, fairly constant and always less than $\pi/4$. Both models also show a high coherency around 6 years. There the phase shift is close to 0 for the model IGFx23 over the time-span 1930-2010. The period range presenting high coherence is less tightened (in particular in the 1960-70's) for the model GGJx22, for which a positive phase shift (less than $\pi/4$) appears from ~ 1980.

It is worth notice that prior to 1940, a significant coherence is found at a period about 5 years, with a relatively weak phase shift. It corresponds to a signal of amplitude less than 0.03 ms (see Fig. 9). This may suggest either changes in the periods of core signals, or decadal modulations of the signals originating from the core. In any case, at such short periods an influence from AAM cannot be disregarded.

3.4.2. Oscillations in the period range 2–5 years over 1948–2021

Motivated by the coherence found at periods shorter than 6 years at early epochs, we performed a dedicated coherence analysis over the more recent era, starting from 1948 onward, when atmospheric reanalyses are available, allowing to clean LOD series from the AAM contribution. Coherent phases are found around 5 and 3.5 years periods between the IGFx23 model and the observations, with a phase shift close to zero (Fig. 12(a)).

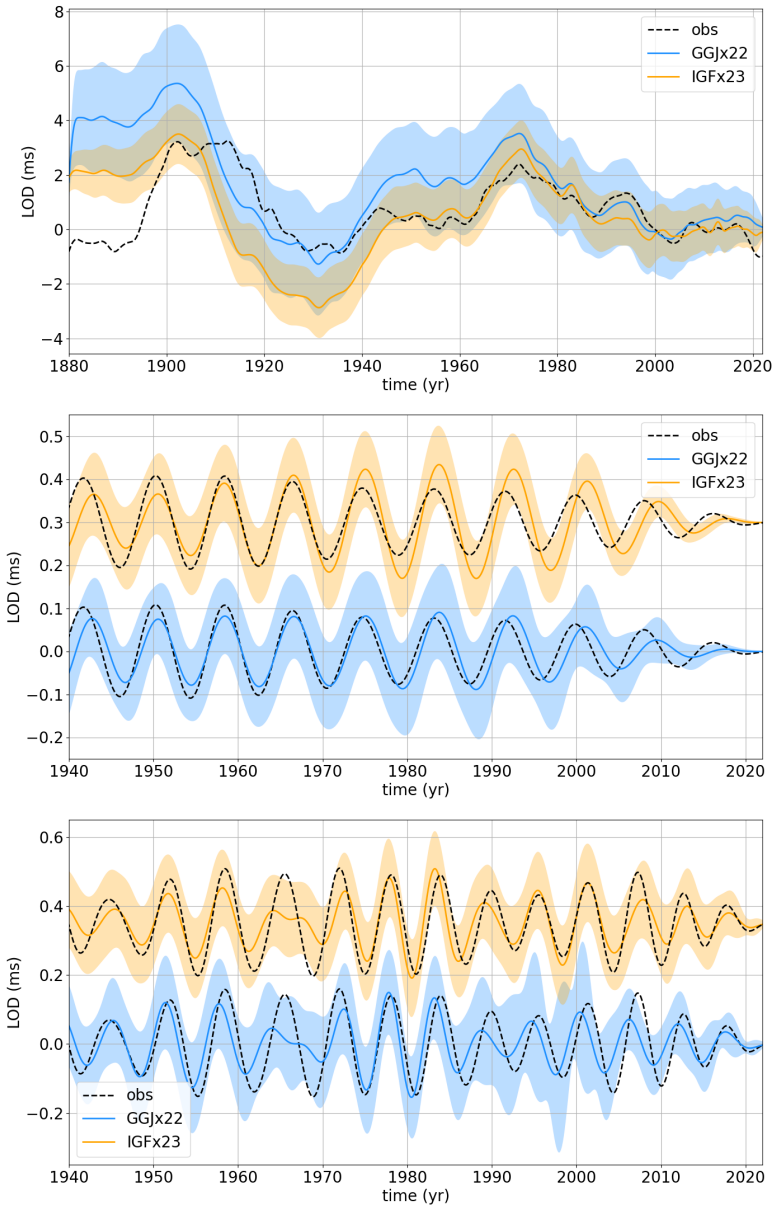

Figure 8: Observed C04 LOD variations (dashed black) and their prediction for the two core flow models IGFx23 (orange) and GGJx22 (blue) – see text for details. Observations were corrected for zonal tides, and atmospheric angular momentum using NCEP model after 1948 only. top: low-pass at periods $T \geq 2$ years. middle: band-pass for periods $7.5 \leq T \leq 9.5$ years. bottom: band-pass for periods $4.5 \leq T \leq 7.5$ years. We applied causal Butterworth filters of order 2. Shaded areas represent the $\pm 1\sigma$ standard deviation within the ensemble of inverted flow models.

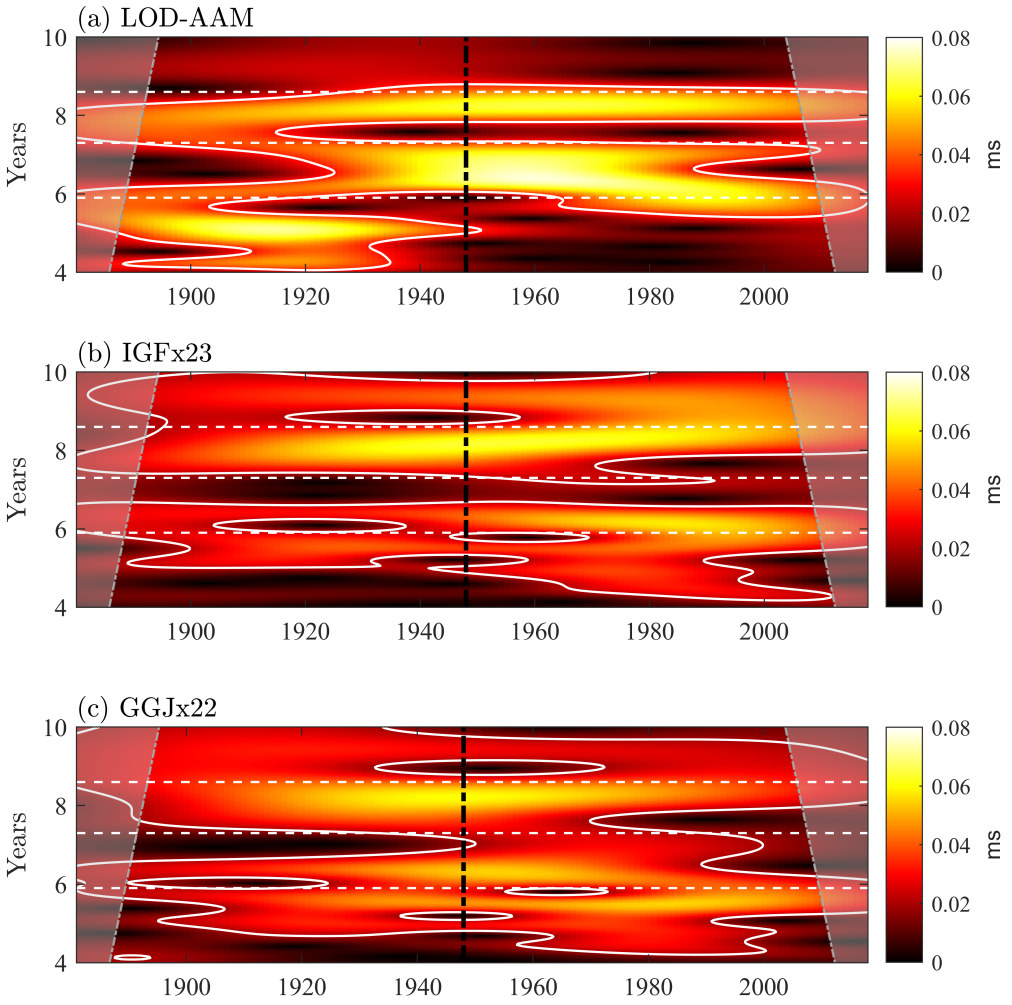

Figure 9: Wavelet analysis for the observed and predicted LOD variations between 1880 and 2021. AAM was corrected only after 1948 (vertical black dashed line) using NCEP model. Scalograms for the observed LOD (a), and the predicted LOD for the IGFx23 model (b) and the GGJx22 model (c). Horizontal white dashed lines correspond to the 5.9, 7.3 and 8.5-year periods. Thin white contour lines correspond to the 95% confidence levels.

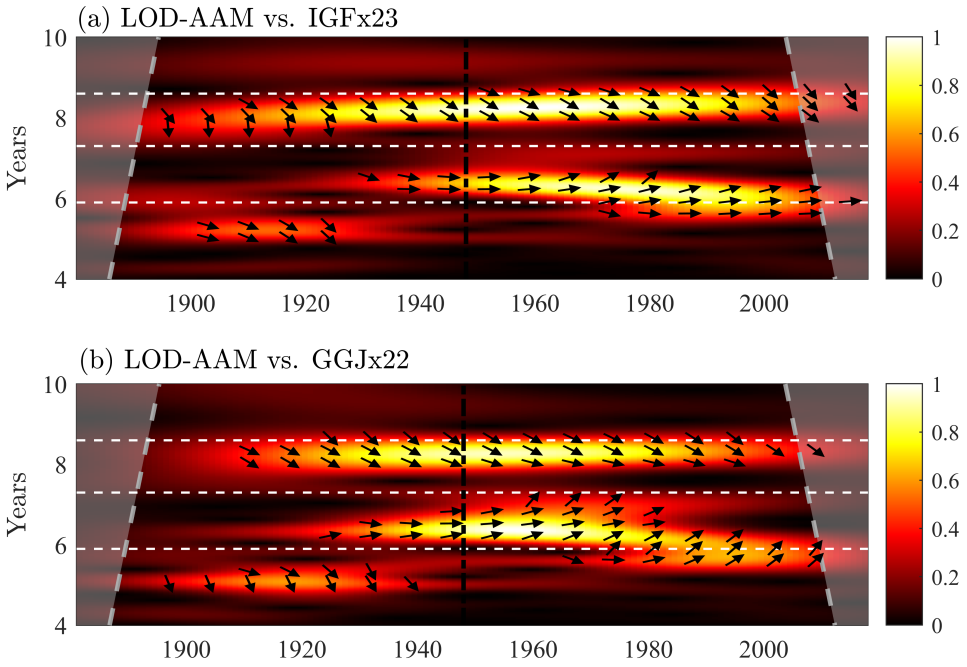

Figure 10: Wavelet coherency and phase diagrams between the observed and predicted LOD variations between 1880 and 2022, for the core flow models IGFx23 (a) and GGJx22 (b), in the period range [4,10] years. AAM was corrected after 1948 only (vertical black dashed line) using NCEP model. Horizontal dashed lines correspond to the 5.9, 7.3 and 8.5-year periods and contour lines correspond to the 95% confidence levels.

The former is observed over the whole time-span, while the latter has a coherence larger than 0.3 from about 1970 onward. Significant coherences, out of phase, are also visible at intermediate periods (about 4.5 years) for this model. The coherence diagram slightly differs for the alternative model GGJx22, which shows predictions approximately in phase with observations at a period around 4.25 years, starting from $\sim$ 1995. The amplitude of the observed (AAM cleaned) LOD at 5 years periods, about 0.02 ms, is over-estimated by both models, as illustrated in Fig. 11. Around 3 to 4 years periods, the observed signal is of the order of 0.01 ms, comparable to what is obtained for the GGJx22 model. The IGFx23 model over-estimates LOD changes at this period, in particular after $\sim$ 1980. It suggests possible high frequency leakage that may be smoothed out in the construction of the CHAOS-7 model (Finlay et al., 2020) used to build model GGJx22 over the past 2 decades, while they would be allowed by the sequential scheme considered by Istas et al. (2023), who built their magnetic field model simultaneously with the flow model. As a matter of fact, interannual LOD predictions from core flow models are sensitive to the considered magnetic data (or field model) from which they derive. In particular the way these handle external magnetic sources (co-estimated, cleaned a priori, or filtered..., see Lesur et al., 2022) might be key in order to properly recover rapid changes in the LOD of core origin.

A closer look at these short periods is available in Fig. 13 where we show the observed and predicted time series over 1962–2022, band-pass filtered at periods between 2 and 4.5 years. Residual LOD changes at these time-scales, once cleaned for AAM, show an amplitude of the order of 0.05 ms. This is a tiny signal, weaker by a factor of about 4 in comparison with the corrected AAM signal in the same period range (see Fig. 9 in Gross et al., 2004). Predictions from both considered flow models show fluctuations of amplitude overall comparable to that of the observed LOD residuals. One may wonder if these just reflect noise in the reconstructed flows, or if they carry some geophysical significance.

Despite relatively large model uncertainties, over the past two decades where geomagnetic observations are the more dense and accurate, the phase of the LOD signal is rather well recovered. This is particularly true for the model GGJx22 inverted from CHAOS-7 since 1999, that captures convincingly about more than 4 consecutive periods. The alternative model IGFx23, inverted at the recent epochs from virtual geomagnetic observatory data, over-estimates the oscillations between 2010-2014, the period covered by the less accurate CryoSat-2 observations (a satellite not dedicated to magnetic records).

4. Summary and discussion

4.1. LOD oscillations in the range 6–9 years

Our analysis confirms the existence of two lines at 6 and 8.5 years in the observed LOD, as first put forward by Duan and Huang (2020). The isolation of these two lines is clearer once subtracted the AAM contribution. Hsu et al. (2021) propose the existence of another line at an intermediate period of 7.3 years. Around $\sim$7-yr our wavelet analysis detects oscillations in hydrological angular momentum functions with an amplitude of the order 0.01 ms (Fig. 4). This signal is likely partly cancelled out by water redistribution (see Fig. 1). A 7 yr signal may be present in LOD series cleaned for the atmospheric contribution only, although from our analysis it does not pass the 95% confidence interval

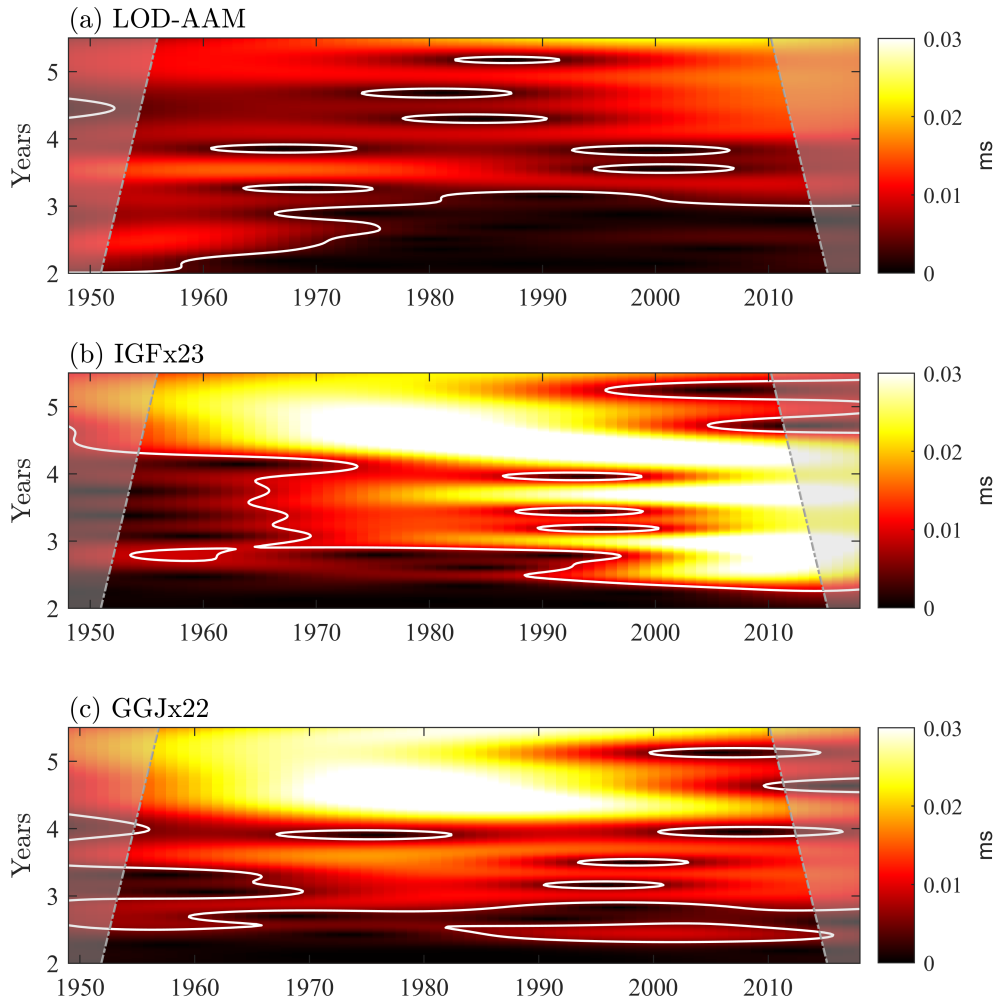

Figure 11: Wavelet analysis between observed (C04 series) and predicted LOD variations, after atmospheric angular momentum correction (using NCEP model), between 1948 and 2021. Scalograms for the observed LOD (a), and for the predicted LOD for IGFx23 (b) and GGJx22 (c) models. Contour lines correspond to the 95% confidence levels.

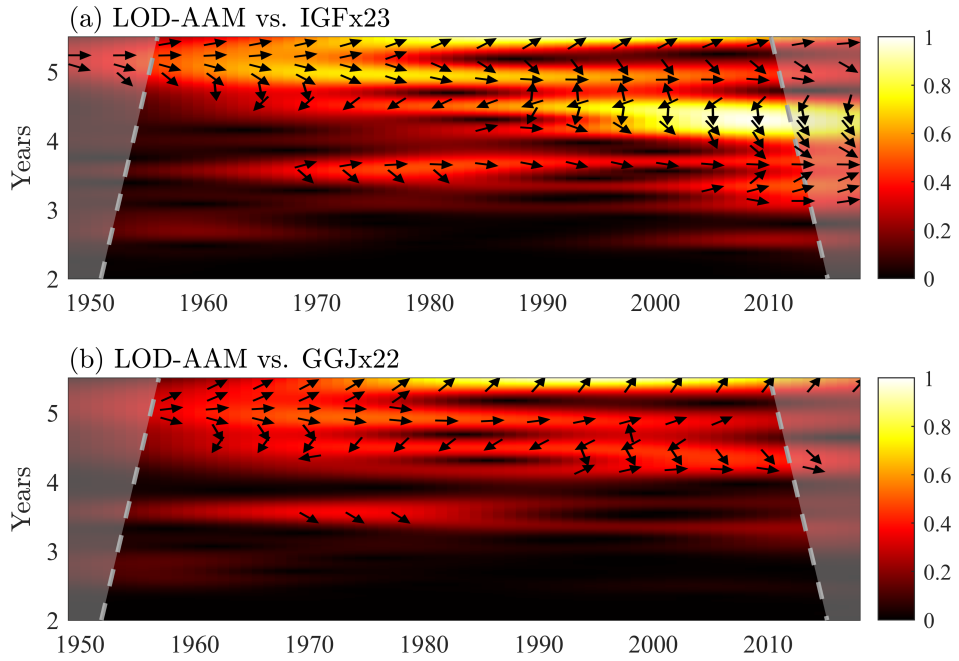

Figure 12: Wavelet coherence analysis between observed (C04 series) and predicted LOD variations, after atmospheric angular momentum correction (using NCEP model), between 1948 and 2021, for the IGFx23 (a) and GGJx22 (b) models.

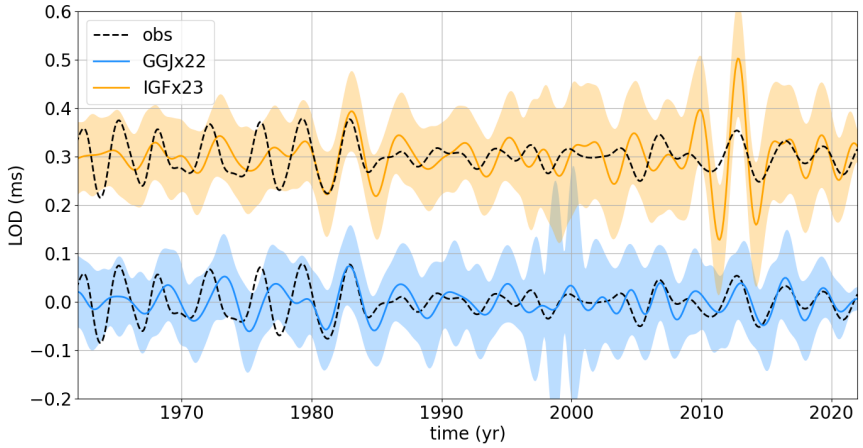

Figure 13: Observed LOD variations (dashed black, C04 series corrected from NCEP AAM) and their prediction for the two core flow models IGFx23 (orange) and GGJx22 (blue), band-pass filtered for periods $2 \leq T \leq 4.5$ years with a causal Butterworth filters of order 2. Observations were corrected for zonal tides, and atmospheric angular momentum using NCEP model.

(Fig. 5). Our tests with synthetic series presenting oscillators at 6 and 8.5 years, but not around 7 years, show the possibility of false positives detection of this latter intermediate spectral line. It is much influenced by the presence of slow LOD changes (the background and a 3rd damped oscillator of decadal period in our synthetic tests). Only longer time-series would help decide whether the apparent ∼7-yr oscillation in LOD is real or not.

We see no evidence either for the presence of a 7-yr line in LOD predictions from core flow models, while clear predicted signals show up at periods around 6 and 8 years (Fig. 9). Furthermore, the coherence analysis of LOD data with the two core flow models does not exhibit any significant coherency around 7 years (Fig. 10), contrary to what is seen around 6 and 8 years.

The nice fit of the amplitude and phase for the SYO and EYO favor a source in the outer core dynamics. It could naturally occur due to the propagation in the fluid core of axisymmetric torsional Alfvén waves (Gillet et al., 2010, 2017) or of quasi-geostrophic magneto-Coriolis waves (Gillet et al., 2022; Istas et al., 2023). These indeed potentially contain an axisymmetric component that may carry angular momentum. They could thus trigger LOD changes over a wide range of frequencies. Such waves have been detected in numerical simulations at parameters approaching Earth's conditions (Aubert et al., 2022). However, contrary to torsional waves, their ability to efficiently couple with the mantle so as to generate detectable angular momentum changes has not yet been proven.

4.2. On possible LOD signals from the core at periods shorter than 5 years

Cleaning for atmospheric contributions much reduces the variance of the LOD signal at periods shorter than 4.5 years (Gross et al., 2004; Duan et al., 2015). The contribution of surface water redistribution (combining sea level changes, hydrology and oceans) to LOD changes is much less than that of the atmosphere at interannual time-scales. Given the limits of the magnetic models on short interannual time-scales (e.g., Ropp et al., 2020), one may wonder if LOD signals associated with core motions are detectable on periods as short as 3 to 4 years. Our wavelet analysis shows two ranges with coherent oscillations around 3.5 and 5 years periods. Their amplitude, of the order of 0.01 ms, is much less than the atmospheric signal that has been removed to the LOD data. We thus cannot yet entirely disregard at this stage a remaining influence from surface envelopes. However, such an amplitude is coherent with tendency of core motions for a weaker energy towards high frequencies (Gillet et al., 2015; Aubert, 2018). Furthermore, the predicted signal correctly predicts the phase (and amplitude, depending on the considered core flow reanalysis) over more than four contiguous oscillations when magnetic data are the more dense and accurate (the past two decades). Here again, one may invoke higher harmonics of torsional modes (see Fig. 8 in Gillet et al., 2017) and/or of magneto-Coriolis modes. Our findings call for further research both regarding the cleaning of external LOD sources, as well as the reanalysis of core motions toward short periods.

Acknowledgments

We thank Richard Holme and an anonymous reviewer for their comments and suggestions which have improved our paper. Discussions with Dominique Jault and Ingo Wardinski have enriched this work. This study is part of the DYNOCORE project which benefits from the CNES financial support through the TOSCA program. This

work has been funded by ESA in the framework of EO Science for Society, through contract 4000127193/19/NL/IA (Swarm + 4D Deep Earth: Core). It has also been partially supported by the French Space Agency (CNES) in the context of the *Swarm* mission of ESA. NG is part of Labex OSUG@2020 (ANR10 LABX56).

Data availability

Effective angular momentum functions were downloaded from https://www.iers.org/IERS/EN/DataProducts/GeophysicalFluidsData/geoFluids.html also available from https://isdc.gfz-potsdam.de/esmdata/ (for series starting in 1976). LOD data were obtained from the Earth orientation center at https://hpiers.obspm.fr/eop-pc/index.php. Flow models are available at https://geodyn.univ-grenoble-alpes.fr/

References

Abarca del Rio, R., Gambis, D., Salstein, D., 2000. Interannual signals in length of day and atmospheric angular momentum, in: Ann. Geophys., Springer. pp. 347–364.

Altamimi, Z., Rebischung, P., Collilieux, X., Métivier, L., Chanard, K., 2023. ITRF2020: an augmented reference frame refining the modeling of nonlinear station motions. Journal of Geodesy 97. doi:10.1007/s00190-023-01738-w.

Aubert, J., 2018. Geomagnetic acceleration and rapid hydromagnetic wave dynamics in advanced numerical simulations of the geodynamo. Geophys. J. Int. 214, 531–547.

Aubert, J., Finlay, C.C., 2019. Geomagnetic jerks and rapid hydromagnetic waves focusing at Earth's core surface. Nature Geoscience 12, 393–398.

Aubert, J., Gillet, N., 2021. The interplay of fast waves and slow convection in geodynamo simulations nearing Earth's core conditions. Geophys. J. Int. 225, 1854–1873.

Aubert, J., Livermore, P.W., Finlay, C.C., Fournier, A., Gillet, N., 2022. A taxonomy of simulated geomagnetic jerks. Geophys. J. Int. doi:10.1093/gji/ggac212.

Barnes, R.T.H., Hide, R., White, A.A., Wilson, C.A., 1983. Atmospheric angular momentum fluctuations, length-of-day changes and polar motion. Proc. R. Soc. London 387, 31–73.

Bizouard, C., Gambis, D., 2009. The Combined Solution C04 for Earth Orientation Parameters Consistent with International Terrestrial Reference Frame 2005. Springer Berlin Heidelberg, Berlin, Heidelberg. pp. 265–270. doi:10.1007/978-3-642-00860-3_41.

Bizouard, C., Lambert, S., Gattano, C., Becker, O., Richard, J.Y., 2019. The IERS EOP 14C04 solution for Earth orientation parameters consistent with ITRF 2014. Journal of Geodesy 93, 621–633. doi:10.1007/s00190-018-1186-3.

Braginskiy, S.I., 1970. Torsional magnetohydrodynamic vibrations in the Earth's core and variations in day length. Geomag. Aeron. 10, 1–8.

Chao, B.F., 2017. Dynamics of axial torsional libration under the mantle-inner core gravitational interaction. J. Geophys. Research: Solid Earth 122, 560–571. doi:https://doi.org/10.1002/2016JB013515.

Chao, B.F., Chung, W., Shih, Z., Hsieh, Y., 2014. Earth's rotation variations: a wavelet analysis. Terra Nova 26, 260–264.

Chulliat, A., Maus, S., 2014. Geomagnetic secular acceleration, jerks, and a localized standing wave at the core surface from 2000 to 2010. J. Geophys. Res. Solid Earth 119, 1531–1543.

Dill, R., 2008. Hydrological model LSDM for operational Earth rotation and gravity field variations. Scientific Technical Report 08/09 GFZ, Potsdam. doi:10.2312/GFZ.b103-08095.

Dobslaw, H., Dill, R., 2018. Predicting Earth Orientation Changes from Global Forecasts of Atmosphere-Hydrosphere Dynamics. Adv. Space Res. 61, 1047–1054. doi:https://doi.org/10.1016/j.asr.2017.11.044.

Dobslaw, H., Dill, R., Grötzsch, A., Brzeziński, A., Thomas, M., 2010. Seasonal polar motion excitation from numerical models of atmosphere, ocean, and continental hydrosphere. J. Geophys. Res.: Solid Earth 115. doi:10.1029/2009JB007127.

Duan, P., Huang, C., 2020. Intradecadal variations in length of day and their correspondence with geomagnetic jerks. Nature Communication 11, 2273. doi:10.1038/s41467-020-16109-8.

549 Duan, P., Liu, G., Hu, X., Hao, X., Huang, Y., Zhang, Z., Wang, B., 2015. Recovery of the 6-year signal
550 in length of day and its long-term decreasing trend. Earth Planets Space 67. doi:10.1186/s40623-015-
551 0328-6.
552 Duan, P.S., Liu, G.Y., Hu, X.G., Sun, Y.F., Li, H.L., 2017. Possible damping model of the 6 year
553 oscillation signal in length of day. Phys. Earth Planet. Inter. 265, 35–42.
554 Evensen, G., 2003. The ensemble Kalman filter: Theoretical formulation and practical implementation.
555 Ocean dynamics 53, 343–367.
556 Finlay, C.C., Kloss, C., Olsen, N., Hammer, M.D., Tøffner-Clausen, L., Grayver, A., Kuvshinov, A.,
557 2020. The chaos-7 geomagnetic field model and observed changes in the south atlantic anomaly.
558 Earth Planets Space 72, 1–31.
559 Finlay, C.C., Olsen, N., Kotsiaros, S., Gillet, N., Tøffner-Clausen, L., 2016. Recent geomagnetic secular
560 variation from Swarm and ground observatories as estimated in the CHAOS-6 geomagnetic field model.
561 Earth Planets Space 68, 1–18.
562 Gillet, N., Gerick, F., Jault, D., Schwaiger, T., Aubert, J., Istas, M., 2022. Satellite magnetic data reveal
563 interannual waves in earth's core. Proc. Natl. Acad. Sci. U.S.A. 119(13). doi:e2115258119.
564 Gillet, N., Huder, L., Aubert, J., 2019. A reduced stochastic model of core surface dynamics based on
565 geodynamo simulations. Geophys. J. Int. 219, 522–539.
566 Gillet, N., Jault, D., Canet, E., 2017. Excitation of travelling torsional normal modes in an Earth's core
567 model. Geophys. J. Int. 210, 1503–1516.
568 Gillet, N., Jault, D., Canet, E., Fournier, A., 2010. Fast torsional waves and strong magnetic field within
569 the Earth's core. Nature 465, 74–77.
570 Gillet, N., Jault, D., Finlay, C., 2015. Planetary gyre, time-dependent eddies, torsional waves, and
571 equatorial jets at the Earth's core surface. J. Geophys. Res.: Solid Earth 120, 3991–4013.
572 Godin, G., 1972. The Analyis of Tides. University of Toronto Press.
573 Grinsted, A., Moore, J.C., Jevrejeva, S., 2004. Application of the cross wavelet transform and wavelet
574 coherence to geophysical time series. Nonlinear Process. Geophys. 11, 561–566.
575 Gross, R., 2015. 3.09 - earth rotation variations – long period, in: Schubert, G.
576 (Ed.), Treatise on Geophysics (Second Edition). second edition ed.. Elsevier, Oxford, pp.
577 215–261. URL: https://www.sciencedirect.com/science/article/pii/B9780444538024000592,
578 doi:https://doi.org/10.1016/B978-0-444-53802-4.00059-2.
579 Gross, R.S., 2001. A combined length-of-day series spanning 1832-1997: LUNAR97. Phys. Earth Planet.
580 Inter. 123, 65–76. doi:10.1016/S0031-9201(00)00217-X.
581 Gross, R.S., Fukumori, I., Menemenlis, D., Gegout, P., 2004. Atmospheric and oceanic excitation of
582 length-of-day variations during 1980–2000. J. Geophys. Res.: Solid Earth 109.
583 Hammer, M.D., Cox, G.A., Brown, W.J., Beggan, C.D., Finlay, C.C., 2021a. Geomagnetic Virtual
584 Observatories: monitoring geomagnetic secular variation with the Swarm satellites. Earth Planets
585 Space 73, 1–22.
586 Hammer, M.D., Finlay, C.C., Olsen, N., 2021b. Applications for CryoSat-2 satellite magnetic data in
587 studies of Earth's core field variations. Earth Planets Space 73, 1–22.
588 Holme, R., De Viron, O., 2013. Characterization and implications of intradecadal variations in length
589 of day. Nature 499, 202–204.
590 Hsu, C.C., Duan, P.S., Xu, X.Q., Zhou, Y.H., Huang, C.L., 2021. On the ∼7 year periodic signal in length
591 of day from a frequency domain stepwise regression method. J. Geod. 95, 55. doi:10.1007/s00190-
592 021-01503-x.
593 Huder, L., Gillet, N., Finlay, C.C., Hammer, M.D., Tchoungui, H., 2020. COV-OBS. x2: 180 years of
594 geomagnetic field evolution from ground-based and satellite observations. Earth Planets Space 72,
595 1–18.
596 Huder, L., Gillet, N., Thollard, F., 2019. pygeodyn 1.1. 0: a Python package for geomagnetic data
597 assimilation. Geoscientific Model Development 12, 3795–3803.
598 IERS Conventions, 2010. IERS Technical note 36, Frankfurt am Main: Verlag des Bundesamts für
599 Kartographie und Geodäsie, p. 179.
600 Istas, M., Gillet, N., Finlay, C.C., Hammer, M.D., Huder, L., 2023. Transient core surface dynamics
601 from ground and satellite geomagnetic data. Geophys. J. Int. accepted.
602 Jault, D., 2003. Electromagnetic and topographic coupling, and LOD variations, in: Jones, C., Soward,
603 A., Zhang, K. (Eds.), Earth's core and lower mantle. Taylor & Francis, London, pp. 56–76.
604 Jault, D., Finlay, C., 2015. Waves in the core and mechanical core-mantle interactions, in: Treatise on
605 Geophysics: Core Dynamics. Elsevier, pp. 225–245.
606 Jungclaus, J.H., Fischer, N., Haak, H., Lohmann, K., Marotzke, J., Matei, D., Mikolajewicz, U., Notz,
607 D., von Storch, J.S., 2013. Characteristics of the ocean simulations in the Max Planck Institute Ocean

Model (MPIOM) the ocean component of the MPI-Earth system model. J. Adv. Model. Earth Syst. 5, 422–446. doi:10.1002/jame.20023.
Lesur, V., Gillet, N., Hammer, M., Mandea, M., 2022. Rapid variations of earth's core magnetic field. Surveys in Geophysics 43, 41–69.
Liu, L., Hsu, H., Grafarend, E.W., 2007. Normal Morlet wavelet transform and its application to the Earth's polar motion. J. Geophys. Res. 112. doi:10.1029/2006JB004895.
Morlet, J., Arens, G., Fourgeau, E., Giard, D., 1982. Wave propagation and sampling theory-Part II, Sampling theory and complex waves. Geophysics 47(2), 222–236.
Mound, J., Buffett, B., 2006. Detection of a gravitational oscillation in length-of-day. Earth Planet. Sci. Lett. 243, 383–389. doi:10.1016/j.epsl.2006.01.043.
Ratcliff, J.T., Gross, R.S., 2022. Combinations of Earth Orientation Measurements: SPACE2021, COMB2021, and POLE2021. JPL Publication URL: https://keof.jpl.nasa.gov/combinations/SpaceCombPole_latest.pdf.
Rekier, J., Chao, B.F., Chen, J., Dehant, V., Rosat, S., Zhu, P., 2022. Earth's Rotation: Observations and Relation to Deep Interior. Surv. Geophys. 43, 149–175. URL: https://doi.org/10.1007/s10712-021-09669-x, doi:10.1007/s10712-021-09669-x.
Ropp, G., Lesur, V., Baerenzung, J., Holschneider, M., 2020. Sequential modelling of the earth's core magnetic field. Earth Planets Space 72, 1–15.
Schaeffer, N., Jault, D., 2016. Electrical conductivity of the lowermost mantle explains absorption of core torsional waves at the equator. Geophys. Res. Lett. 43, 4922–4928.
Stephenson, F.R., Morrison, L.V., Whitrow, G.J., Hide, R., Wilkins, G.A., McCrea, W.H., Message, P.J., Runcorn, S.K., 1984. Long-term changes in the rotation of the Earth : 700 B.C. to A.D. 1980. Phil. Trans. Royal Soc. London. Series A, Mathematical and Physical Sciences 313, 47–70. doi:10.1098/rsta.1984.0082.
Torrence, C., Compo, G., 1998. A Practical Guide to Wavelet Analysis. Bull. Am. Meteorol. Soc. 79, 61–78.
Wunsch, C., Heimbach, P., Ponte, R., Fukumori, I., the ECCO-GODAE Consortium Members, 2009. The global general circulation of the ocean estimated by the ECCO-consortium. Oceanography 22, 88–103.
Yaglom, A.M., 1962. An introduction to the theory of stationary random functions. Prentice-Hall.
Yan, H., Chao, B.F., 2012. Effect of global mass conservation among geophysical fluids on the seasonal length of day variation. J. Geophys. Res. 117. doi:10.1029/2011JB008788.

Appendix A. Supplementary information

Hundred random realizations of the synthetic LOD series, as described in Section 2.2.1, have been carried out. We illustrate here the influence of the high-pass filtering with a cut-off period of 10 yr (Fig. A.1). We also show the CWT when there is no long-period background in the synthetic time-series, for a single oscillator of period 6 years, or two oscillators of periods 6 and 8.5 years (Fig. A.2). Two other realizations for the synthetic case with two oscillators and a background plus noise are also provided (Fig. A.3).

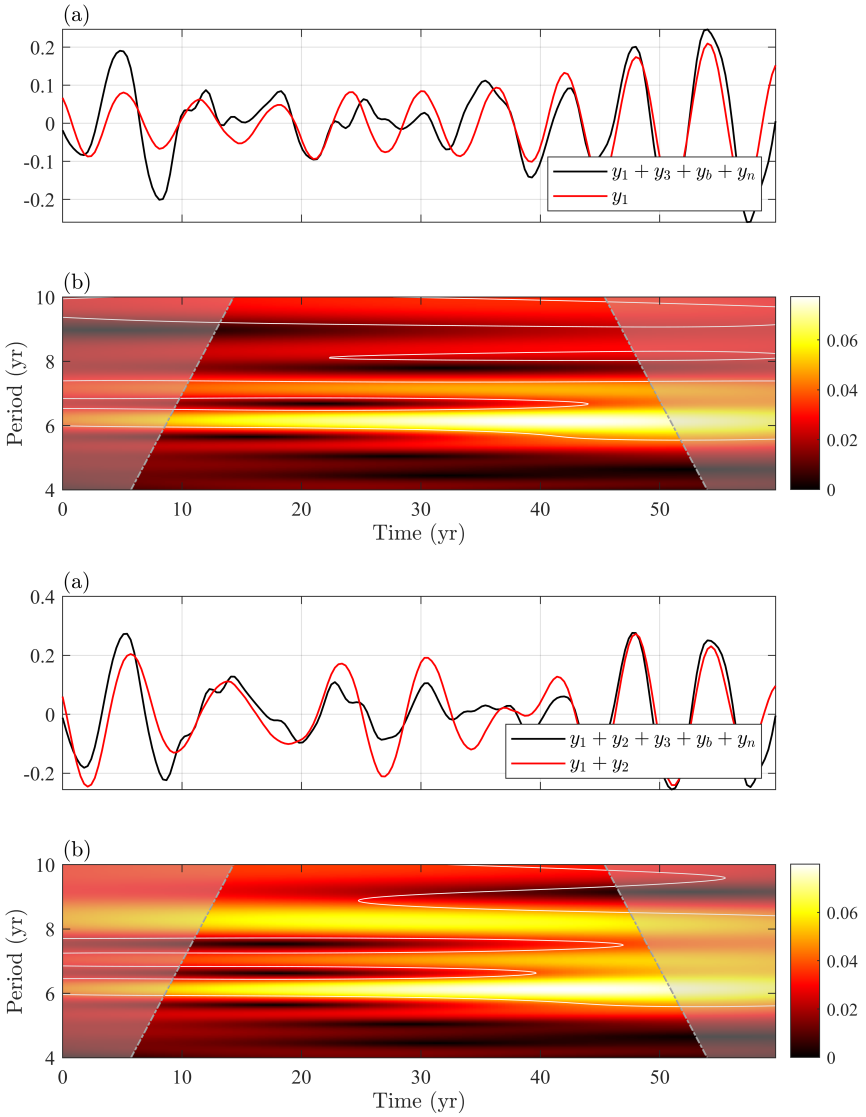

Figure A.1: High-pass filtered synthetic signal composed of an auto-regressive stochastic background (y_b), a colored noise (y_n), and various oscillators. Top: two damped oscillators at 6 and 17 years periods, with $Q = 20\pi$ and $Q = \pi$ (y_1 and y_3). Bottom: three damped oscillators at 6, 8.5 and 17 years periods, with $Q = 20\pi, 20\pi$ and π respectively (y_1, y_2 and y_3). (a) Time series, (b) Continuous Wavelet Transform.

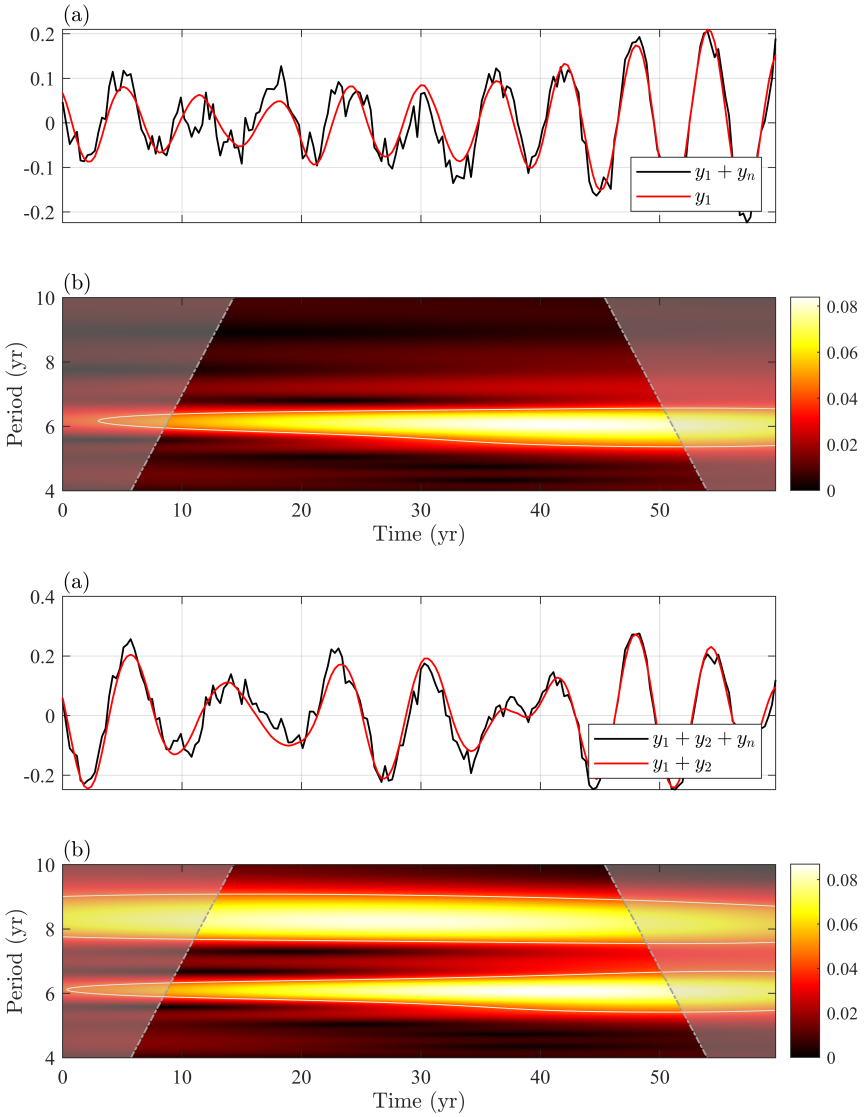

Figure A.2: Synthetic signals in the absence of a background, embedded in colored noise (y_n). Top: one damped oscillator of period 6 years, with $Q = 20\pi$ (y_1). Bottom: two damped oscillators of periods 6 and 8.5 years, both with $Q = 20\pi$ (y_1 and y_2). (a) Time series, (b) Continuous Wavelet Transform.

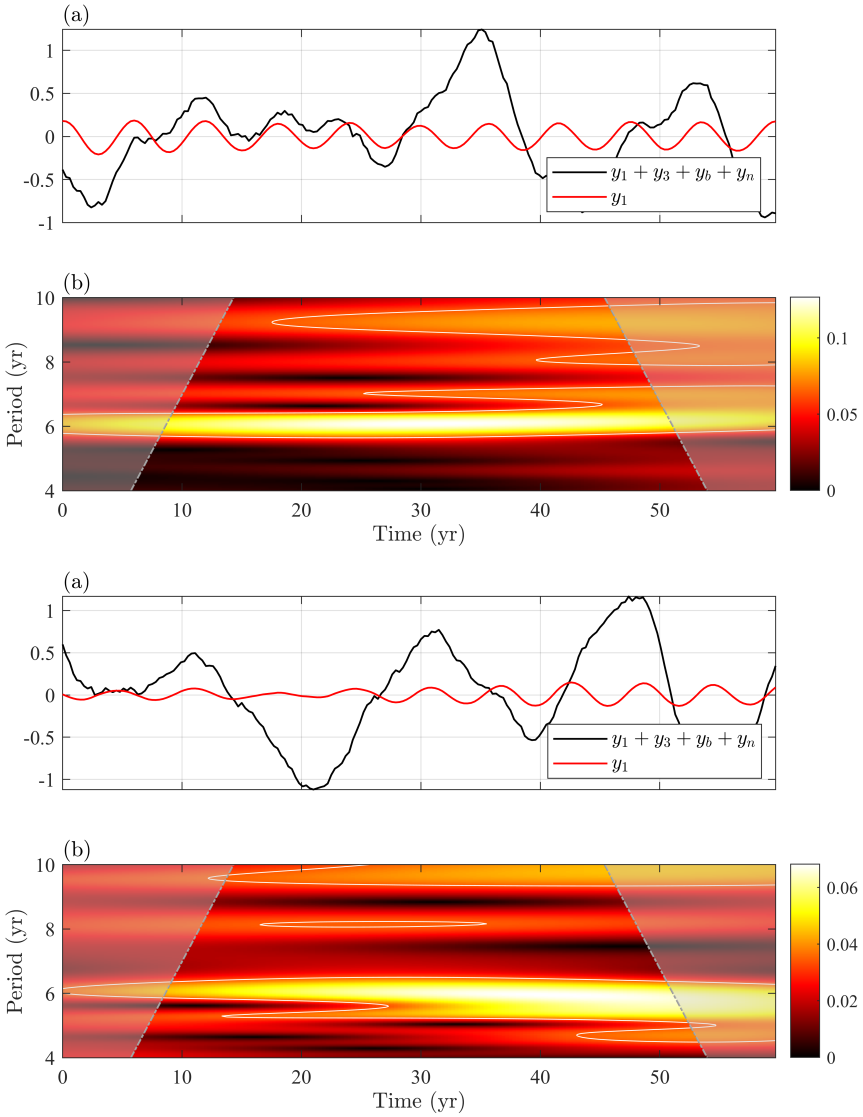

Figure A.3: Two other realizations of a synthetic signal composed of an auto-regressive stochastic background (y_b) plus two damped oscillators at 6 and 17-yr periods, with $Q = 20\pi$ and $Q = \pi$ (y_1 and y_3) embedded in colored noise (y_n). (a) Time series, (b) Continuous Wavelet Transform.